

Article

Numerical Analysis of Dynamic Response and Liquefaction Phenomena in Sandy Seabed Foundation around a Semi-Circular Breakwater under Wave Loading

Junwei Liu ^{1,*}, Yunping Jia ¹, Lin Cui ¹ , Honglei Sun ², Xu Lv ³ and Mohsen Saleh Asheghabadi ¹

¹ School of Civil Engineering, Qingdao University of Technology, Qingdao 266525, China; 17806290521@163.com (Y.J.); cuiilin@qut.edu.cn (L.C.); mohsen@qut.edu.cn (M.S.A.)

² Institute of Geotechnical Engineering, Zhejiang University of Technology, Hangzhou 310059, China; sunhonglei@zju.edu.cn

³ China Petroleum & Chemical Corporation, Changsha 410153, China; lvxu2020@163.com

* Correspondence: liujunwei@qut.edu.cn; Tel.: +86-150-6619-8828

Abstract: Understanding the stability of the seabed foundation holds paramount significance in guaranteeing the safety and structural soundness of the breakwater alongside additional offshore structures. This study aimed to investigate the stability of a sandy seabed foundation around a semi-circular breakwater under wave loading in nearshore areas. A coupled numerical model of waves, a semi-circular breakwater, and the seabed was developed based on the OpenFOAM platform. The VARANS equations were used to govern the wave behavior. Meanwhile, the Biot's partially dynamic model was employed to numerically simulate the seabed response considering both consolidation under self-weight and dynamic response under wave loading. The effects of various wave parameters, seabed properties, and the radius of the structure on the dynamic response of the seabed and the depth of liquefaction were investigated. The numerical results indicate that an increase in wave height, period, and permeability coefficient intensifies the dynamic response of the seabed soil. Furthermore, an increase in water depth weakened the soil's dynamic response. There was a negative correlation between the radius of the semi-circular breakwater and the dynamic response. The influence of Poisson's ratio on the dynamic response of the seabed was relatively small. Furthermore, a stronger dynamic pore pressure response was observed at the connection between the semi-circular breakwater and the rubble foundation.

Keywords: semi-circular breakwater; wave loading; dynamic response of the seabed; liquefaction



Citation: Liu, J.; Jia, Y.; Cui, L.; Sun, H.; Lv, X.; Asheghabadi, M.S. Numerical Analysis of Dynamic Response and Liquefaction Phenomena in Sandy Seabed Foundation around a Semi-Circular Breakwater under Wave Loading. *J. Mar. Sci. Eng.* **2024**, *12*, 40. <https://doi.org/10.3390/jmse12010040>

Academic Editor: Abdellatif Ouahsine

Received: 3 November 2023

Revised: 11 December 2023

Accepted: 16 December 2023

Published: 23 December 2023



Copyright: © 2023 by the authors. Licensee MDPI, Basel, Switzerland. This article is an open access article distributed under the terms and conditions of the Creative Commons Attribution (CC BY) license (<https://creativecommons.org/licenses/by/4.0/>).

1. Introduction

With the continuous development of the maritime industry, new requirements are constantly being proposed for the design and construction of breakwaters. The development of new types of breakwaters has become a significant topic in coastal engineering, among which, semi-circular breakwaters have emerged as an innovative coastal protective structure [1]. A semi-circular breakwater consists of a reinforced concrete arc-shaped structure and a bottom plate, situated on a rubble foundation. The decision to incorporate wave-dissipating openings, referred to as wave-dissipating holes, on the side facing the waves can be made based on specific needs to decrease wave reflection and wave forces. Moreover, openings can be created on both the wave-facing and leeward sides of the breakwater to facilitate the exchange of seawater.

Throughout the service life of the breakwater, it encounters intricate marine environments. Marine structures are subject to not only substantial wind and wave loading, but they also often rest upon recently deposited, loosely compacted soil layers with a low bearing capacity. Under periodic loading, these soil layers are prone to instability, resulting in structural damage and a reduced service life. The previous literature has documented

occurrences of breakwater damage due to soil liquefaction [2–4]. Therefore, gaining a more comprehensive comprehension of the seabed dynamic response and accurate prediction of potential liquefaction zones near the breakwater have evolved into pivotal factors in the design and maintenance of marine structures, especially under cyclic wave loading and in the presence of new types of breakwaters.

In the initial stages of researching such topics, analytical solutions are often employed [5–7]. However, these analytical solutions assume that breakwaters exist as impermeable straight lines, neglecting the influence of their geometry and characteristics on wave propagation, as well as the effect of the breakwater's self-weight on the initial stress distribution of the seabed foundation. Compared to theoretical analytical methods, physical model tests can effectively address these issues. Mizutani et al. [8] conducted model tests with submerged breakwaters to investigate the interaction between regular waves, breakwaters, and seabed soil. Building on their research, Mostafa et al. [9] investigated the dynamic response of the seabed under composite breakwaters, presenting a BEM-FEM (Boundary Element Method–Finite Element Method) model that considered the influence of caisson deformation. Further research has been conducted through physical model tests by Oumeraci [10] and Sumer et al. [11]. Additionally, due to advancements in computer technology, numerical simulations have been widely employed. Mase et al. [12] developed a numerical model based on the Biot consolidation equation to investigate the distribution of effective stress and pore pressure near composite breakwaters and rubble breakwaters under standing wave conditions. Jeng et al. [13] developed a 2D finite element model based on previous research to investigate the pore water pressure near composite breakwaters, with the maximum pore water pressure occurring at the interface between the caisson and the rubble foundation. Elsafti et al. [14] conducted an investigation into the self-rotational displacement of breakwaters and the dynamic response of surrounding seabed soil under wave action.

Numerous scholars worldwide have conducted comprehensive numerical simulation studies on the interactions between waves, breakwaters, and seabed soil. Zhang Jisheng et al. obtained an improved two-dimensional (2D) numerical model by improving the ultra-static pore pressure accumulation Sassa model [15]. Zheng Dongsheng et al. developed an integrated model (PORO-WSSI II) for wave–seabed–structure interactions (WSSI) and found that under the action of wave loads, there is a dense fluid exchange between the water and the seabed, and there is a strong seepage force in the seabed. An excessive upward seepage force leads to seabed liquefaction [16]. Cui Lin et al. established an integrated 3D model of wave–seabed–structure interactions, and studied the liquefaction and settlement of breakwater heads at estuaries [17].

Many studies on the interactions between waves, breakwaters, and the seabed mainly focus on vertical breakwaters [18–20]. As coastal engineering continues to progress, there remains a dearth of research on emerging breakwater designs. In this study, we developed a numerical model for assessing the dynamic response of the seabed using OpenFOAM. By coupling existing fluid models, a comprehensive numerical framework for studying the interaction among waves, a semi-circular breakwater, and the seabed was established. The numerical model was validated, indicating its accuracy and applicable to the wave–breakwater–seabed interaction problem. The shape and size of the breakwater in the numerical model were designed with reference to the semi-circular breakwater in the South Channel Phase I Project of the Yangtze River Estuary Navigation Improvement Project. The effects of different wave heights, periods, water depths, permeability coefficients, Poisson's ratios, and breakwater radius on the pore water pressures, effective stresses, and liquefaction depths in the seabed soils near semi-circular breakwaters were investigated in order to investigate the dynamic response of the seabed foundations near semi-circular breakwaters and the liquefaction of the seabed foundation near them under the action of wave loads.

2. Numerical Model

2.1. Flow Model

The flow model is based on the olaFlow solver within OpenFOAM, used to simulate the generation and propagation of waves, as well as their interaction with breakwater structures. The fluid in the model is assumed to be incompressible and continuous. Fluid movement and seepage in porous media are governed by the VARANS equation, which follows the laws of conservation of mass and conservation of momentum.

$$\frac{\partial \langle u_i \rangle}{\partial x_i} = 0 \tag{1}$$

$$\frac{\partial \rho \langle u_i \rangle}{\partial t} + \frac{\partial}{\partial x_j} \left[\frac{1}{\Phi} \rho \langle u_i \rangle \langle u_j \rangle \right] = -\Phi \frac{\partial \langle p^* \rangle^f}{\partial x_i} + \Phi g_j \chi_j \frac{\partial \rho}{\partial x_i} + \frac{\partial}{\partial x_j} \left[\mu_{\text{eff}} \frac{\partial \langle u_i \rangle}{\partial x_j} \right] - [\text{CT}] \tag{2}$$

where $[\text{CT}] = A \langle u_i \rangle + B |\langle u \rangle| \langle u_i \rangle + C \frac{\partial \langle u_i \rangle}{\partial t}$.

The coefficients A and B were proposed by Englund [21] and the specific formulas are shown in Equations (3) and (4).

$$A = \alpha \frac{(1 - \phi)^3}{\phi^2} \frac{\mu}{D_{50}^2} \tag{3}$$

$$B = \beta \left(1 + \frac{7.5}{\text{KC}} \right) \frac{1 - \phi}{\phi^2} \frac{\rho}{D_{50}} \tag{4}$$

where ρ is density, and u_i is velocity vector. p^* , g_j , ϕ , and D_{50} are the pseudo-dynamic pressure, gravitational acceleration, porosity of the material, and average equivalent particle size of the material, respectively. The symbol X represents the position vector. Moreover, μ_{eff} is the effective dynamic viscosity, which considers both the molecular motion viscosity and the turbulent effect ($\mu_{\text{eff}} = \mu + \rho \nu_t$). Here, the value of ν_t is the turbulent motion viscosity, determined by the selected turbulence model; the k- ϵ turbulence model was used in this study.

The VOF method was employed within the flow model to accurately capture the free surface. Each grid cell in the calculation domain consists of water and air, and α is used to represent the water volume per unit volume in each grid. A value of $\alpha = 1$ indicates a cell entirely occupied by water, while $\alpha = 0$ signifies a cell entirely occupied by air. When α assumes a value between 0 and 1, it implies a cell containing a mixture of both water and air. Within the monomer, alterations in fluid properties are comprehensively described through the indicator function α , which is utilized as follows:

$$\Phi = \alpha \Phi_{\text{water}} + (1 - \alpha) \Phi_{\text{air}} \tag{5}$$

where Φ_{water} is the nature of water and Φ_{air} is the nature of air.

In numerical simulation and physical flume tank tests, due to limitations in calculation conditions and test site size, waves are affected and reflected as they propagate to the boundary, resulting in the generation of reflected waves [22,23]. The wave model for this numerical simulation was solved using the olaFlow solver, and the active wave absorption method was used at the outlet boundary of the wave model to eliminate wave reflection. In addition, taking 3–5 times the wavelength as the length of the flow field, but only taking the result of the middle stable region, in this region, the wavefront diagram is basically stable and the influence of reflected waves can be ignored.

2.2. Seabed Model

Assuming that both pore water and soil skeleton in porous media are compressible, and considering the effect of displacement acceleration of soil particles, the seabed soil is assumed to be isotropic. Additionally, and also considering that fluid flow in porous media follows Darcy’s law of permeability, a porous elastic seabed model was established,

incorporating the soil inertia term based on the u-p formulation of the Biot equation [24]. The governing equation for the dynamic response of the seabed soil is presented below:

$$\frac{\partial p_e^2}{\partial x^2} + \frac{\partial p_e^2}{\partial y^2} + \frac{\partial p_e^2}{\partial z^2} - \frac{\gamma_w n_s \beta}{k_s} \frac{\partial p_e}{\partial t} + \rho \frac{\partial \varepsilon_s^2}{\partial t^2} = \frac{\gamma_w}{k_s} \frac{\partial \varepsilon_s}{\partial t} \quad (6)$$

where x , y , and z are the axes of the Cartesian coordinate system. t , k_s , and p_e are time, the permeability coefficient of the seabed soil, and the oscillating pore water pressure within the seabed soil caused by waves, respectively. γ_w denotes the heaviness of water, n_s is the porosity of the soil, and ρ is the average density of the porous seabed, which is calculated using the following equation:

$$\rho = \rho_f n_s + \rho_s (1 - n_s) \quad (7)$$

where ρ_s is the seabed soil density, ρ_f represents the pore water density, ε_s denotes the soil volumetric strain, and β is the pore water compressibility, where ε_s and β can, respectively be expressed as follows:

$$\varepsilon_s = \frac{\partial u_s}{\partial x} + \frac{\partial v_s}{\partial y} + \frac{\partial w_s}{\partial z} \quad (8)$$

where u_s , v_s , and w_s are the displacements of the soil particles in the x , y , and z directions, respectively.

$$\beta = \frac{1}{K'} = \frac{1}{K_w} + \frac{1 - S_r}{P_{w0}} \quad (9)$$

where K' is the apparent bulk modulus of water, S_r is the saturation of the soil, P_{w0} is the absolute pressure of water, and K_w is the true bulk modulus of water, taken as $1.95 \times 10^9 \text{ N/m}^2$.

The relationship between the pore water pressure and the effective stress is:

$$\frac{\sigma'_{sx}}{\partial x} + \frac{\partial \tau_{sxy}}{\partial y} + \frac{\partial \tau_{sxz}}{\partial z} = \frac{\partial p_e}{\partial x} \quad (10)$$

$$\frac{\partial \tau_{sxy}}{\partial x} + \frac{\sigma'_{sy}}{\partial y} + \frac{\partial \tau_{syz}}{\partial z} = \frac{\partial p_e}{\partial y} \quad (11)$$

$$\frac{\partial \tau_{sxy}}{\partial x} + \frac{\partial \tau_{syz}}{\partial y} + \frac{\sigma'_{sz}}{\partial z} = \frac{\partial p_e}{\partial y} \quad (12)$$

where σ'_{sx} , σ'_{sy} , and σ'_{sz} are the normal stress of the soil in the x , y , and z directions, and τ_{sxy} , τ_{syz} , and τ_{syz} are the shear stress component of the soil in the x , y and z directions, respectively. Normal stress is the stress perpendicular to the same cross-section. The normal stress here is a positive compression.

Assuming that the seabed soil is a homogeneous elastic material, the stress–strain relationship satisfies the generalized Hooke’s law according to the theory of linear elasticity:

$$\sigma'_{sx} = 2G \left[\frac{\partial u_s}{\partial x} + \frac{\mu}{1 - 2\mu} \varepsilon_s \right] \quad (13)$$

$$\sigma'_{sy} = 2G \left[\frac{\partial v_s}{\partial y} + \frac{\mu}{1 - 2\mu} \varepsilon_s \right] \quad (14)$$

$$\sigma'_{sz} = 2G \left[\frac{\partial w_s}{\partial z} + \frac{\mu}{1 - 2\mu} \varepsilon_s \right] \quad (15)$$

$$\tau_{sxz} = G \left[\frac{\partial u_s}{\partial z} + \frac{\partial w_s}{\partial x} \right] = \tau_{szx} \quad (16)$$

$$\tau_{syz} = G \left[\frac{\partial v_s}{\partial z} + \frac{\partial w_s}{\partial y} \right] = \tau_{szy} \quad (17)$$

$$\tau_{sxy} = G \left[\frac{\partial u_s}{\partial y} + \frac{\partial v_s}{\partial x} \right] = \tau_{syx} \tag{18}$$

where G is the shear modulus of the soil, and the relationship between G and elastic modulus E is:

$$G = \frac{E}{2(1 + \mu)} \tag{19}$$

where μ is the Poisson’s ratio. Bringing Equations (12)–(17) into (9)–(11), the relationship between displacement and pore pressure in the seabed soil is:

$$G\nabla^2 u_s + \frac{G}{(1 - 2\mu)} \frac{\partial \varepsilon_s}{\partial x} = \frac{\partial p_e}{\partial x} + \rho \frac{\partial^2 u_s}{\partial t^2} \tag{20}$$

$$G\nabla^2 v_s + \frac{G}{(1 - 2\mu)} \frac{\partial \varepsilon_s}{\partial y} = \frac{\partial p_e}{\partial y} + \rho \frac{\partial^2 v_s}{\partial t^2} \tag{21}$$

$$G\nabla^2 w_s + \frac{G}{(1 - 2\mu)} \frac{\partial \varepsilon_s}{\partial z} = \frac{\partial p_e}{\partial z} + \rho \frac{\partial^2 w_s}{\partial t^2} \tag{22}$$

where $\nabla^2 = \frac{\partial^2}{\partial x^2} + \frac{\partial^2}{\partial y^2} + \frac{\partial^2}{\partial z^2}$ is the Laplacian Operator.

2.3. Model Coupling and Boundary Conditions

The fluid model and the seabed model are coupled together using a one-way coupling algorithm, which relies on the continuity of pressure at the common interface between the two models. The fluid model was employed to simulate the generation, propagation, and interaction of waves with the structure. By solving the VARANS equation and the VOF equation, the fluid model provides information such as the velocity field, free surface elevation, and dynamic water pressure at the fluid–structure interface. On the other hand, the seabed model was used to capture the consolidation process under the self-weight of the structure and the dynamic response under wave loading. The dynamic wave pressure at the bottom of the fluid model is applied to the seabed surface. By iteratively solving the governing equations of the seabed model, the dynamic response of the seabed soil is computed, and the corresponding results are obtained [25]. To illustrate a more intuitive depiction of the one-way coupling between the fluid model and the seabed model, the computational process of the wave–structure–seabed system at every time step is presented in Figure 1.

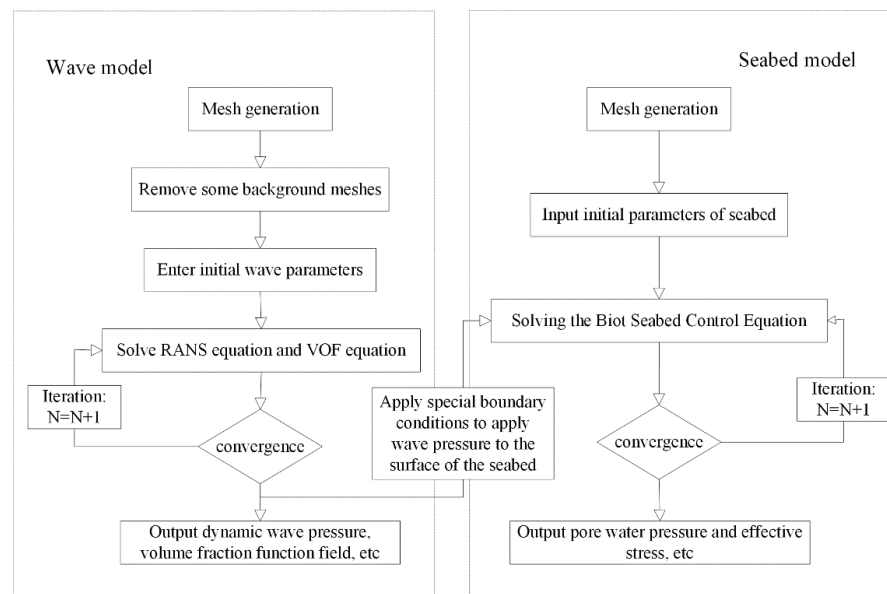


Figure 1. Numerical model coupling process.

Boundary conditions play a significant role in determining the behavior and performance of structures and soils in marine environments [26]. Boundary conditions clearly influence variations in pressures, forces, displacements, and other variables related to structures and soils [27]. In general, there are various methods for defining border conditions in order to extract meaningful results based on them [28,29]. Based on the specific boundary conditions, the governing equations of the seabed model are solved to obtain the dynamic response of the surrounding seabed soil under wave loading for the semi-circular breakwater. The boundary conditions for the seabed computational domain are set as follows in Figure 2:

(1) At the sea bed surface (i.e., at $z = h$), it is commonly assumed that there are no vertical effective normal stresses and shear stresses. The pore water pressure at this location is equal to the dynamic pressure applied on the seabed surface due to wave loading:

$$\sigma'_{sz} = \tau_{sxz} = 0, p_e = p_s \tag{23}$$

(2) At the lower boundary of the seabed (i.e., at $z = 0$), it is generally assumed to be an impermeable rigid bedrock, i.e., no displacement in the horizontal and vertical directions and no vertical seepage:

$$u_s = v_s = w_s = 0, \frac{\partial p_e}{\partial z} = 0 \tag{24}$$

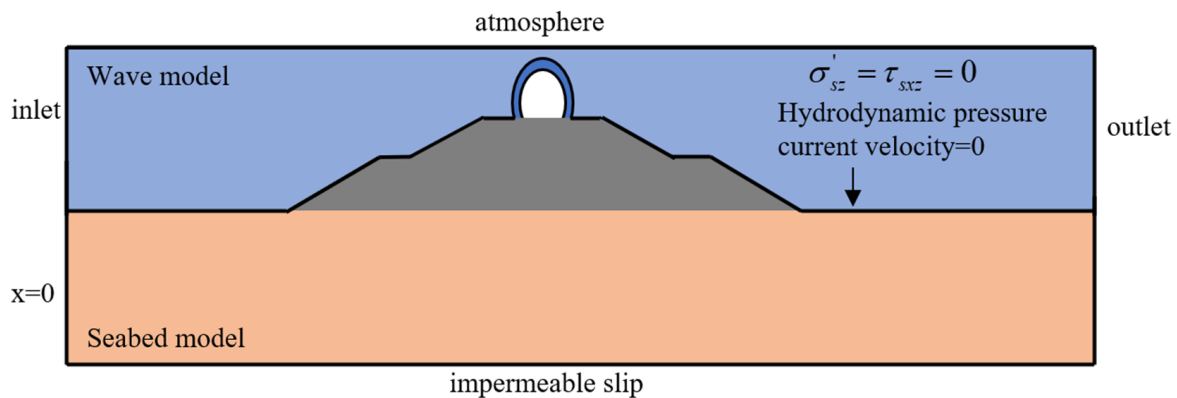


Figure 2. Numerical domain.

3. Model Validation

3.1. Mesh Convergence Verification

To ensure the accuracy and efficiency of the model calculations, a convergence test was performed on the grid resolution. Figures 3 and 4 show the temporal variations in the wave surface and the pore water pressure under different grid resolutions. The specific parameters used in the wave model and seabed model are as follows: wave height $H = 0.03$ m, wave period $T = 1.4$ s, water depth $d = 0.21$ m, seabed thickness $h = 0.2$ m, saturation degree $Sr = 0.99$, shear modulus $G = 1 \times 10^8$ Pa, Poisson’s ratio = 0.33, porosity = 0.3, and permeability coefficient = 2.2×10^{-3} m/s. The grid size $\Delta x = L/150$, $\Delta z = H/20$ was selected to balance time and cost constraints while ensuring the accuracy of the calculations. In the calculation process, the grid size required for wave model convergence is significantly smaller than that for the seabed model. However, considering the presence of the breakwater and aiming to enhance calculation precision, this study used grid sizes that are identical in both the wave model and the seabed model. Based on the results of the time step test, the time step in the wave model was set to 0.001 s, while in the seabed model, the time step was set to 0.01 s.

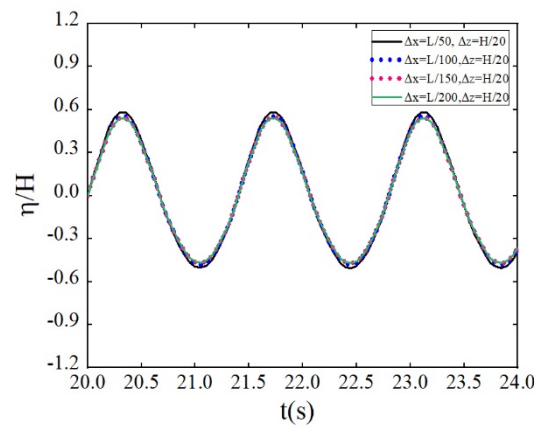


Figure 3. Free surface time history curve at a point in the wave model with different grid densities.

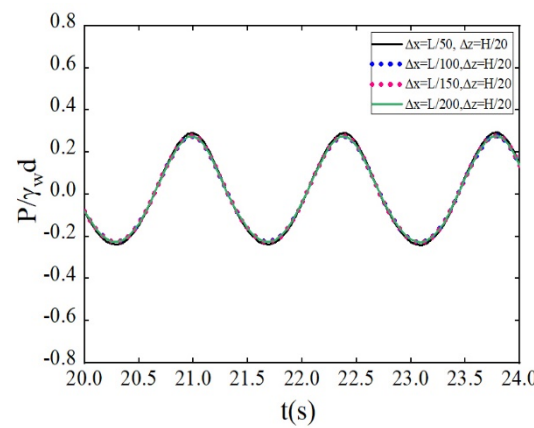


Figure 4. Pore water pressure variation curve with time at a point in the wave model with different grid densities.

3.2. Model Validation with Wave Flume Test

Mizutani et al. [8] conducted a series of laboratory experiments to study the interactions between waves, the seabed, and the breakwater. The experimental setup is depicted in Figure 5: the left side represents the wave generation area, and the right side represents the wave dissipation area. A submerged breakwater was placed on the seabed, and sensors were installed at locations A, B, C, and D to record the pore pressure. Wave gauges were placed at locations a, b, c, and d to measure the wave height. Table 1 presents the values of the wave, seabed soil, and breakwater parameters used in Mizutani’s laboratory experiments.

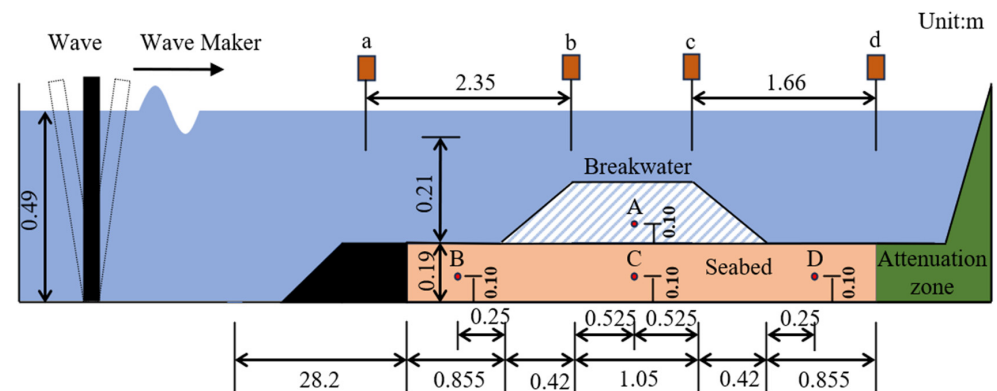


Figure 5. Mizutani et al. [8] sink test schematic.

Table 1. Parameters used in the Mizutani et al. flume test.

Parameter	Value	Unit
Wave parameters	Wave Height (H)	0.03
	Period (T)	1.4
	Water Depth (d)	0.21
Seabed Parameters	Seabed Thickness (h)	0.2
	Saturation (Sr)	0.99
	Shear Modulus (G)	1.0×10^8
	Poisson's Ratio (ν)	0.33
	Porosity (ϕ)	0.3
	d_{50}	0.001
	Hydraulic Conductivity (k_s)	2.2×10^{-3}
Breakwater	Saturation (Sr)	0.99
	Shear Modulus (G)	1.0×10^9
	Poisson's Ratio (ν)	0.24
	Porosity (ϕ)	0.33
	d_{50}	0.03
	Hydraulic Conductivity (k_s)	1.8×10^{-7}
	Armor Slope	1:2

Figures 6 and 7 illustrate the comparison between the numerical simulation results in this study and the experimental results of Mizutani et al. regarding wave profiles and pore water pressure at various seabed points under wave action. In Figure 6, it is evident that the numerical simulation results closely match the experimental results at points a and b in front of the breakwater. Meanwhile, at points c and d located behind the breakwater, the wave experienced attenuation processes. These characteristics are clearly reflected in the experimental results of Mizutani et al., and the numerical simulation results in this study also captured these features. While there exists some numerical discrepancy when compared to the experimental results, the overall trend of the wave profile remains in substantial agreement, indicating the reliability of the fluid model used in this study. Figure 7 shows that the simulated curves of pore water pressure in the sandy seabed under wave loading at points A, B, C, and D correspond closely to the monitoring results of Mizutani et al.'s experiments. This demonstrates that the seabed model employed in this study is suitable for simulating the interaction between waves, the seabed, and breakwaters.

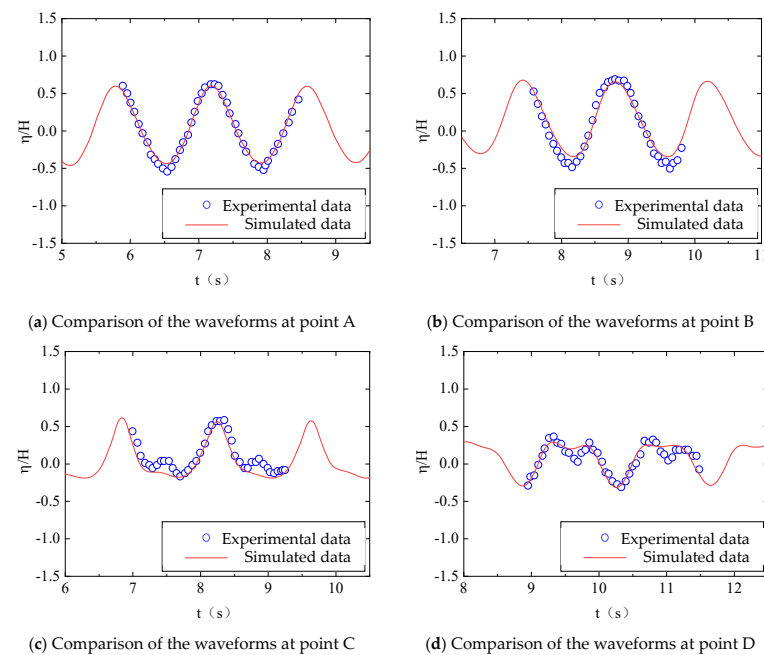


Figure 6. Comparison of the waveforms between numerical simulation results in this study and the experimental results of Mizutani et al. [8].

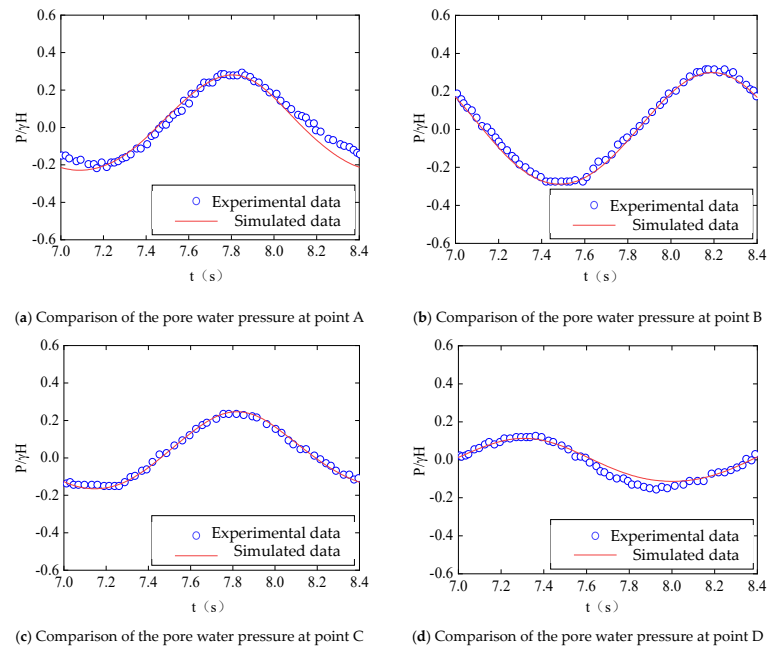


Figure 7. Comparison of the pore water pressure between numerical simulation results and the experimental results.

4. Results and Discussion

4.1. Parameter Setting

The shape and size of the semi-circular breakwater were designed with consideration of the semi-circular breakwater size utilized in the South Channel Phase I Project of the Yangtze River Estuary Navigation Improvement Project. Previous studies have indicated that the presence of openings in the breakwater does not have a significant influence on wave attenuation under high water levels. Given that this study concentrated on submerged breakwaters with high water levels, the design of the semi-circular components in the actual engineering can be simplified. The frontal view of the semi-circular breakwater model is shown in Figure 8. The breakwater consisted of an upper semi-circular component, a lower plate section, and a layer of rubble. The width of the rubble was 44.8 m, the outer diameter of the semi-circular component was 5 m, the inner diameter was 4.5 m, and the length of the lower straight section was 1.5 m. The coordinate origin was located at the seabed’s center, with wave propagation occurring along the positive x -axis. The numerical wave flume’s length (L_s) was set at four times the wavelength.

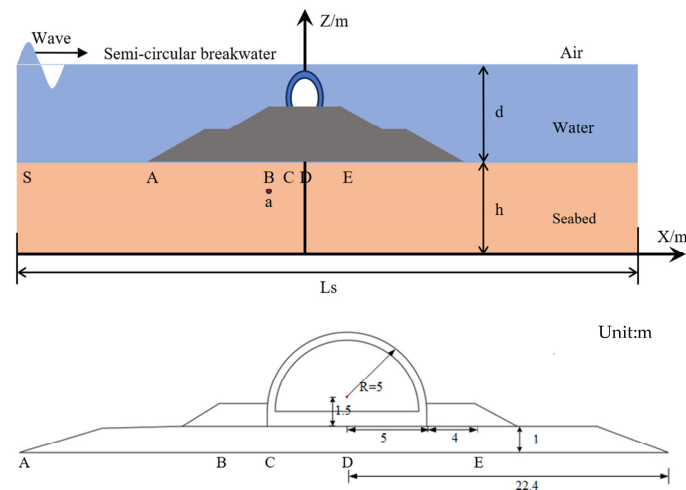


Figure 8. The sketch of the numerical set-up.

According to the research conducted by Jeng et al. [13], it has been shown that relatively high pore water pressures exist at the toe of the rubble foundation, at the interface between the breakwater and the rubble foundation, and below the center of the caisson. Therefore, this study concentrated on investigating the dynamic response of the seabed at points A, C, and D. The parameters for the waves, breakwater, and seabed are listed in Table 2.

Table 2. Parameters used in the numerical studies.

	Parameter	Value	Unit
Wave parameters	Wave Height (H)	1.25	m
	Period (T)	8	s
	Water Depth (d)	7.5	m
Seabed Parameters	Seabed Thickness (h)	20	m
	Saturation (Sr)	0.98	
	Shear Modulus (G)	1.0×10^7	N/m ²
	Poisson’s Ratio (ν)	0.33	
	Porosity (ϕ)	0.425	
	Hydraulic Conductivity (k_s)	1×10^{-3}	m/s
Rubble Bed	Elastic Modulus (E)	1.2×10^8	N/m ²
	Hydraulic Conductivity (k_s)	0.005	m/s
	Porosity (ϕ)	0.333	
	Density (ρ)	2200	Kg/m ³
	Poisson’s Ratio (ν)	0.25	
Breakwater	Elastic Modulus (E)	5.5×10^8	N/m ²
	Hydraulic Conductivity (k_s)	0	m/s
	Porosity (ϕ)	0	
	Density (ρ)	2500	Kg/m ³
	Poisson’s Ratio (ν)	0.25	

4.2. Effect of Wave Characteristics

In this section, we investigate the influence of wave characteristics on the dynamic response of the seabed. The wavelength is directly affected by the wave period and water depth, and changes in these three variables directly affect the wave loads acting on the seabed surface, consequently influencing the stability of the seabed.

Figures 9 and 10 show the distribution curves of the maximum pore water pressure and maximum effective stress concerning the seabed depth at points A, C, and D for different wave heights (i.e., 0.5 m, 1.25 m, 2 m). In Figure 9, it is evident that the maximum pore water pressure at the same seabed depth significantly increased with increasing wave height. This occurs because larger wave heights result in more substantial wave energy impacting the seabed surface, intensifying the dynamic response of the seabed around the semi-circular breakwater and leading to a significant increase in pore water pressure. This effect was more particularly prominent in shallow seabed areas, specifically within the range of $0.8 < z/h < 1$. In regions where $z/h < 0.8$, the influence was less significant, which is also the reason why liquefaction under wave loading tends to occur in shallow seabed regions. As the seabed depth increases, wave energy propagates and dissipates within the seabed, leading to a gradual decrease in pore water pressure. The maximum pore water pressure decreased most rapidly within a depth range of approximately 4 m below the seabed surface, followed by a slower decrease. Furthermore, among points A, C, and D, it became evident that the maximum pore water pressure was situated at point C, aligning with the interface between the semi-circular breakwater and the rubble foundation. This consistency corresponds to the conclusions drawn by Jeng et al. [13]. This phenomenon might be attributed to the modified drainage conditions within the foundation soil, induced by the presence of the semi-circular breakwater, along with the heightened wave reflection and superposition effects near this vicinity. Consequently, this region experienced elevated wave heights and stronger dynamic pore pressure response in the seabed.

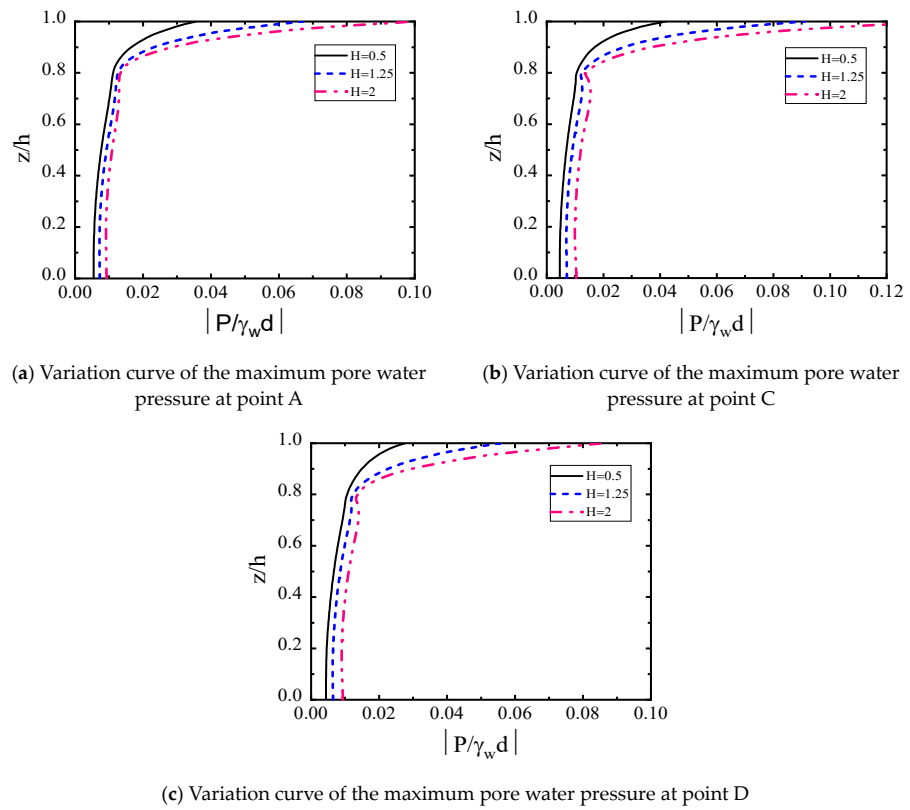


Figure 9. Variation curve of the maximum pore water pressure with depth at each measurement point around the semi-circular breakwater at different wave heights.

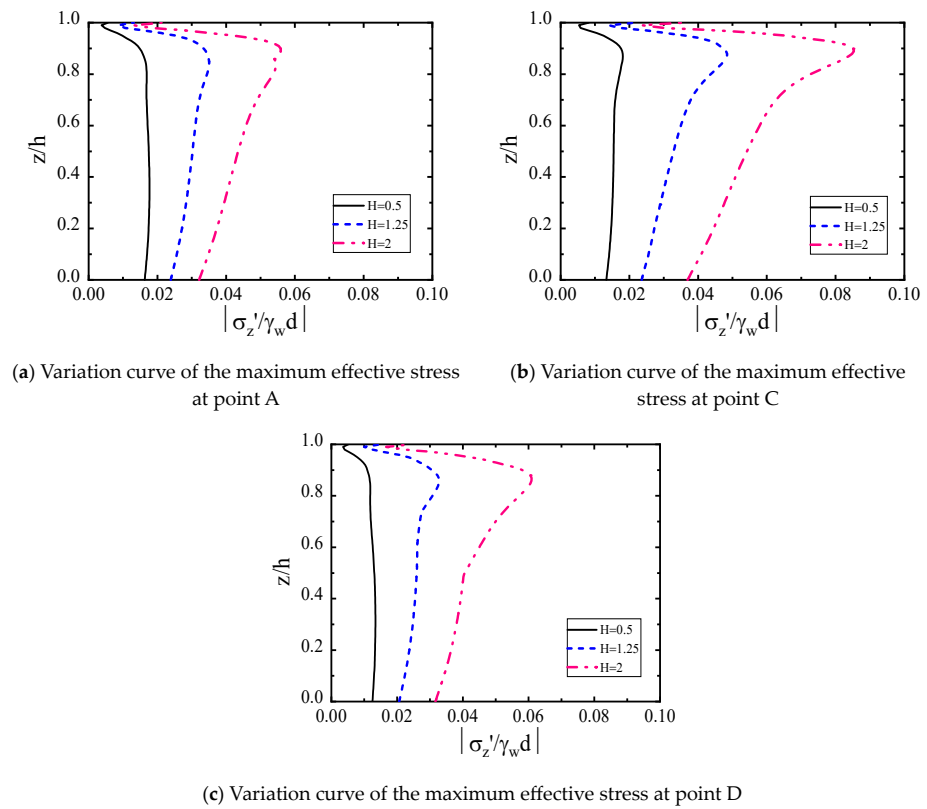


Figure 10. Variation curve of the maximum value of effective stress with depth at each measurement point around the semi-circular breakwater at different wave heights.

Figure 10 reveals that the influence of wave height on the maximum vertical effective stress in the soil around the semi-circular breakwater resembles that of the pore water pressure. The maximum vertical effective stress at the same seabed depth increased with increasing wave height. Among points A, C, and D, point C exhibited the greatest variation in maximum vertical effective stress with wave height, followed by point D, while point A showed the smallest variation. This is due to point A experiencing weaker wave reflection and superposition effects, followed by point D, with point C experiencing the strongest effects. Similar to the maximum pore water pressure, the sudden change in the maximum vertical effective stress occurred at approximately $z/h = 0.8$. Within the range of $0.8 h < z < h$, the maximum vertical effective stress was relatively small. According to the effective stress principle, this range is more susceptible to experience seabed liquefaction according to the criteria for transient liquefaction assessment.

The wave periods considered in this study were 6 s, 8 s, and 10 s. Figures 11 and 12 illustrate the distribution of the maximum pore water pressure and maximum vertical effective stress at different points around the semi-circular breakwater for different wave periods. From the figures, it is evident that the maximum pore water pressure and maximum vertical effective stress in the seabed at the same depth increased with longer wave periods. This occurs because the wave period is closely related to the wave length, and as the wave period increases, so does the wave length. A larger wave length contains more energy, leading to an amplified energy input on the seabed surface and intensifying the dynamic response of the seabed.

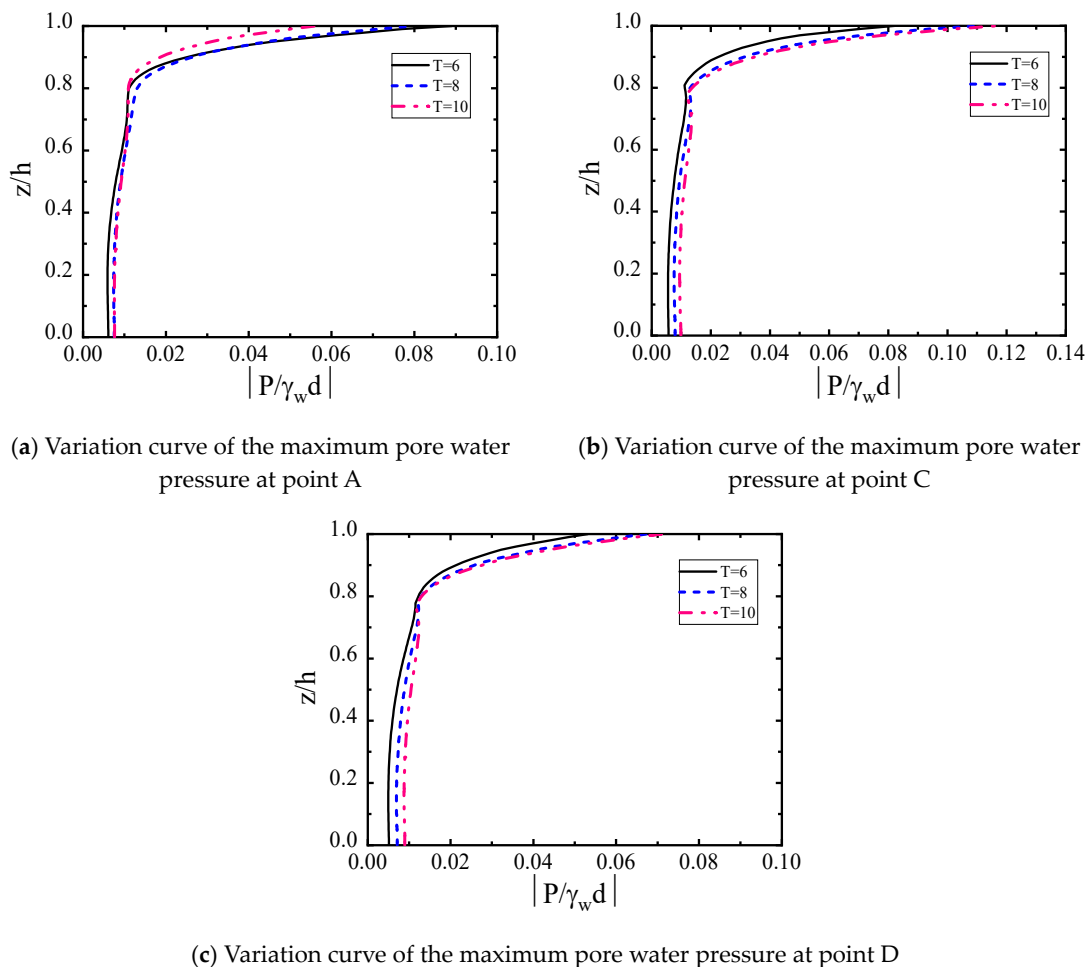


Figure 11. Variation curve of the maximum pore water pressure with depth at each measurement point around the semi-circular breakwater at different periods.

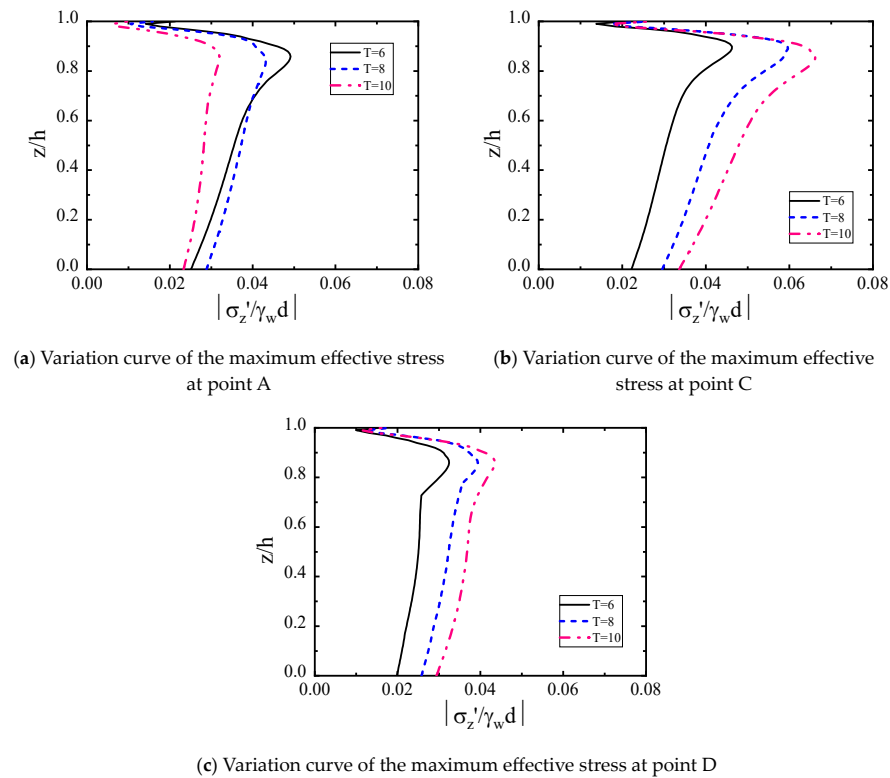


Figure 12. Variation curve of the maximum value of effective stress with depth at each measurement point around the semi-circular breakwater at different periods.

Figures 11 and 12 show that the alterations in the wave period impact both the maximum vertical effective stress and maximum pore water pressure at the same seabed depth, with variations occurring around $z = 0.8 h$. Within the interval of $0 < z < 0.8 h$, both the maximum pore water pressure and maximum vertical effective stress exhibited a gradual increase. In the range of $0.8 h < z < h$, the rate of increase became more rapid. Notably, the maximum pore water pressure tended to increase significantly in this region. Similarly, the maximum vertical effective stress also showed an increasing trend within the range of $0 < z < 0.8 h$, reaching its peak value at a depth of approximately $0.8 h$. In the range of $0.8 h < z < h$, the maximum vertical effective stress decreased as it approached the seabed surface. This indicates that the seabed is more prone to experience transient liquefaction in this region.

The variation in dynamic response due to changes in wave period follows a similar pattern to that observed for wave height. Point C showed the most significant variation, followed by point D, while point A showed the weakest dynamic response among the three points (A, C, and D).

The water depths considered were 5, 7.5, and 10 m. Figures 13 and 14 show the maximum values of the pore water pressure and vertical effective stress at each measurement point at different water depths around the semi-circular breakwater respectively. Upon analyzing Figures 13 and 14, it can be seen that the maximum pore water pressure and the maximum vertical effective stress decreased as water depth increased while maintaining the same seabed depth. This decline can be attributed to the reduction in wave pressure exerted upon the seabed surface due to heightened water depth, subsequently leading to the diminishment of both pore water pressure and vertical effective stress within the seabed soil. Furthermore, the analysis revealed that in cases of a shallow water depth, the maximum vertical effective stress of the seabed soil underwent more noticeable and rapid changes along the depth distribution of the seabed. When the water depth reached 10 m, the pore water pressure within the range of $0 < z < 0.8 h$ remained almost constant.

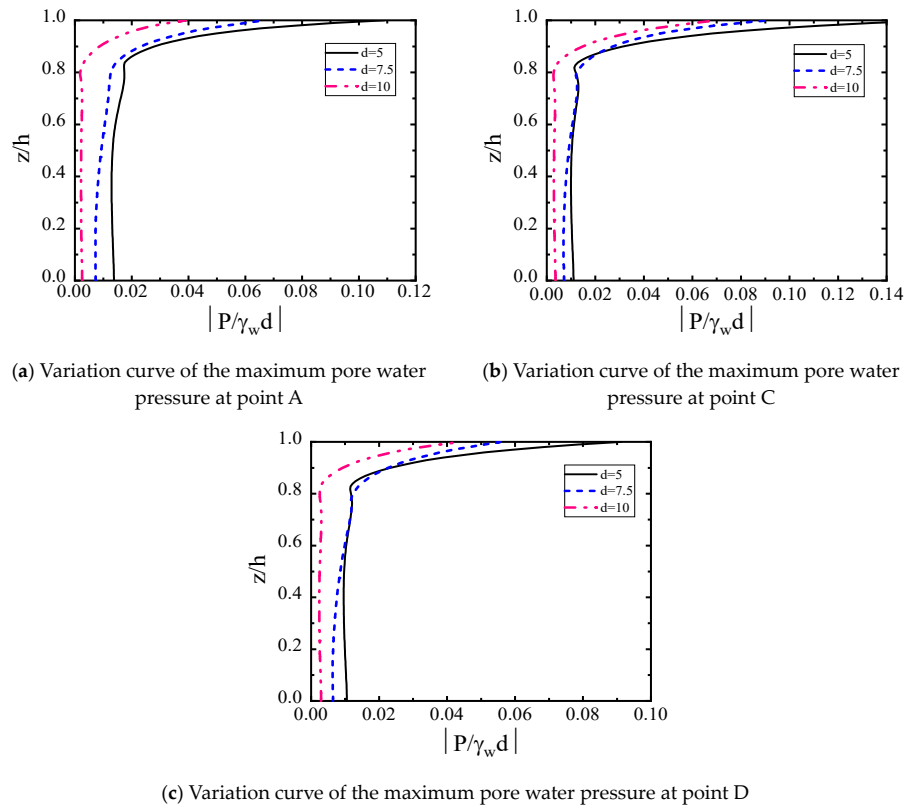


Figure 13. Variation curve of the maximum pore water pressure with depth at each measurement point around the semi-circular breakwater at different water depths.

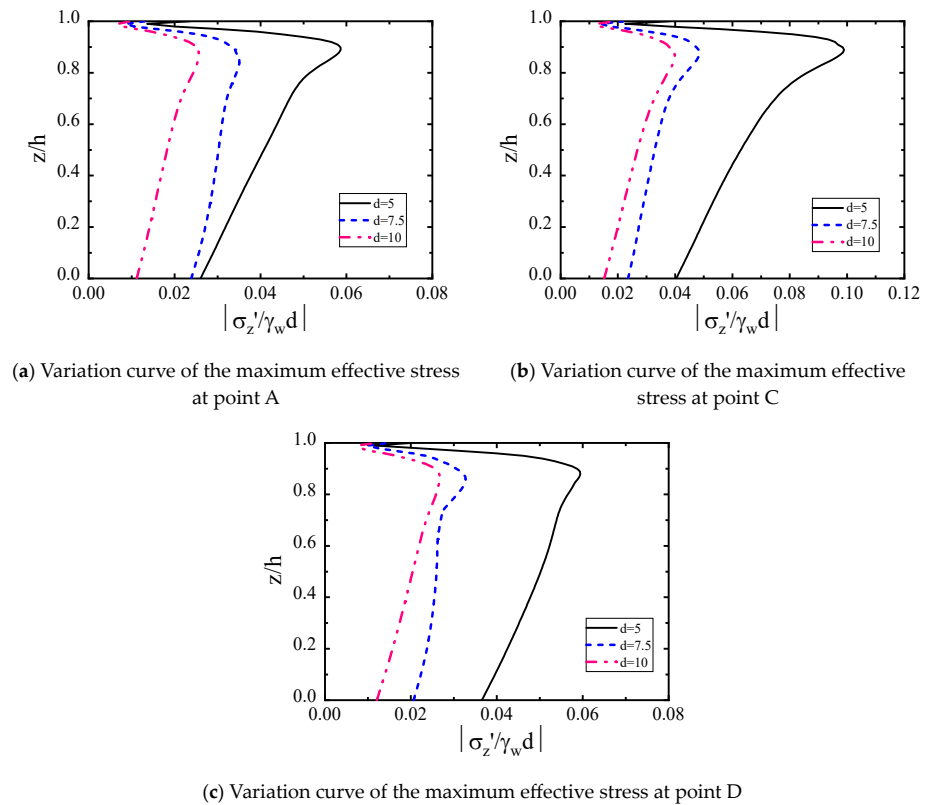


Figure 14. Variation curve of the maximum value of effective stress with depth at each measurement point around the semi-circular breakwater at different water depths.

4.3. Sea Bed Characteristics

Compared to the effects of wave characteristics, changes in the physical properties of the seabed will directly influence the distribution of the pore water pressure and vertical effective stress in the seabed. This section focuses on the effect of soil permeability and Poisson’s ratio variation on the dynamic response of the seabed.

Figures 15 and 16 illustrate the variations in the maximum pore water pressure and maximum vertical effective stress within the seabed at specified points A, C, and D, as a function of depth, for permeability coefficients of 0.0001 m/s, 0.001 m/s, and 0.01 m/s. As shown in Figures 15 and 16, the maximum pore water pressure within the seabed at the same depth increased as the permeability coefficient increased. As the depth of the seabed increased, the maximum pore water pressure gradually decreased. It tended to stabilize as it approached the bottom of the seabed. Furthermore, as the depth of the seabed increased, the decay rate of the maximum pore water pressure under different permeability coefficients varied at different locations. For a permeability coefficient of $k_s = 0.0001$ m/s, the decay rate diminished around $z = 0.9$ h. In the case of $k_s = 0.001$ m/s, the attenuation rate dropped at $z = 0.8$ h. In situations where $k_s = 0.01$ m/s, the attenuation rate did not exhibit a significant inflection point, as the change in the permeability coefficient directly impacted the fluid flow within the seabed pores. The increase in permeability coefficient led to an increase in the fluid velocity in the soil pores. Among the three points A, C, and D, the dynamic response at point C was the strongest. As shown in Figure 16, it is evident that at the same seabed depth, the maximum vertical effective stress decreased with the increase in the permeability coefficient. As the seabed’s depth increased, the effective stress experienced a gradual increase, and its peak appeared near the seabed’s surface. The smaller the permeability coefficient, the closer its peak was to the surface of the seabed. Across the various measurement points near the semi-circular breakwater, the vertical effective stress reached its maximum at the interface between the breakwater and the riprap foundation.

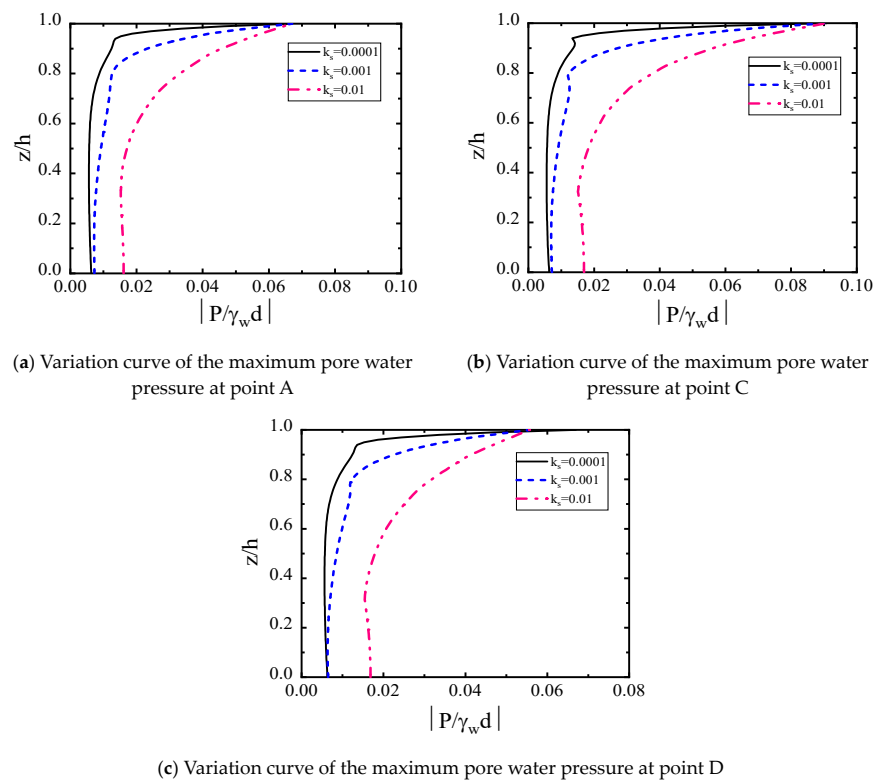


Figure 15. Variation curve of the maximum pore water pressure with depth at each measurement point around the semi-circular breakwater with different levels of soil permeability.

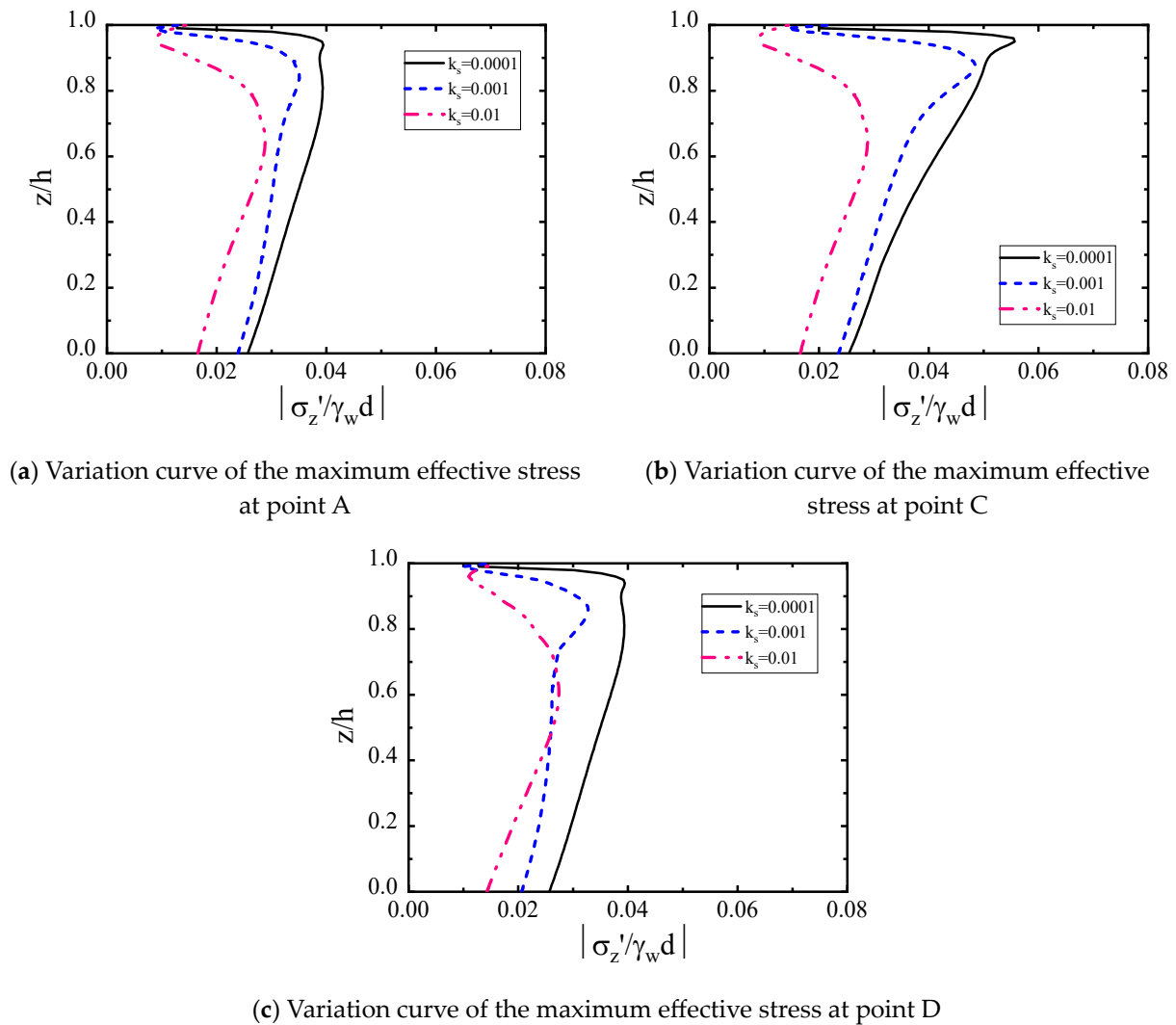


Figure 16. Variation curve of the maximum value of effective stress with depth at each measurement point around the semi-circular breakwater with different levels of soil permeability.

Figures 17 and 18 show the variations in the maximum pore water pressure and maximum vertical effective stress with depth for different Poisson’s ratios (i.e., 0.2, 0.3, 0.4) in the seabed. As depicted in Figure 17, it is evident that the maximum pore water pressure in the seabed soil at the same depth can be divided into two parts as the Poisson’s ratio changes: in the range of $0 < z < 0.8 h$, the maximum pore water pressure decreased with an increase in the Poisson’s ratio; in the range of $0.8 h < z < h$, the variation in the Poisson’s ratio minimally impacted the pore water pressure, and the maximum values remained almost the same for all Poisson’s ratios at the same depth. Analyzing Figure 18, it becomes apparent that the maximum vertical effective stress in the seabed soil decreased with an increase in the Poisson’s ratio at the same depth. It initially increased and subsequently decreased as the seabed depth increased, peaking at $z = 0.8 h$. In comparison to the influences of wave characteristics and soil permeability coefficients on the dynamic response of the seabed, the effect of the Poisson’s ratio on the seabed’s dynamic response was relatively small.

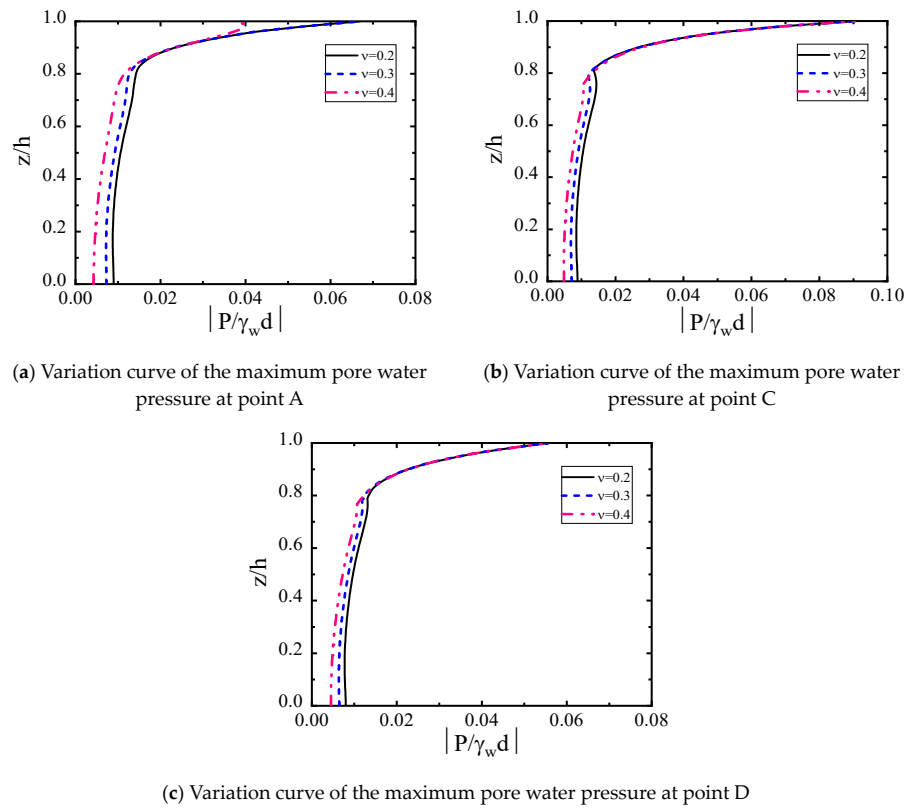


Figure 17. Variation curve of the maximum pore water pressure with depth at each measurement point around the semi-circular breakwater with different Poisson's ratios.

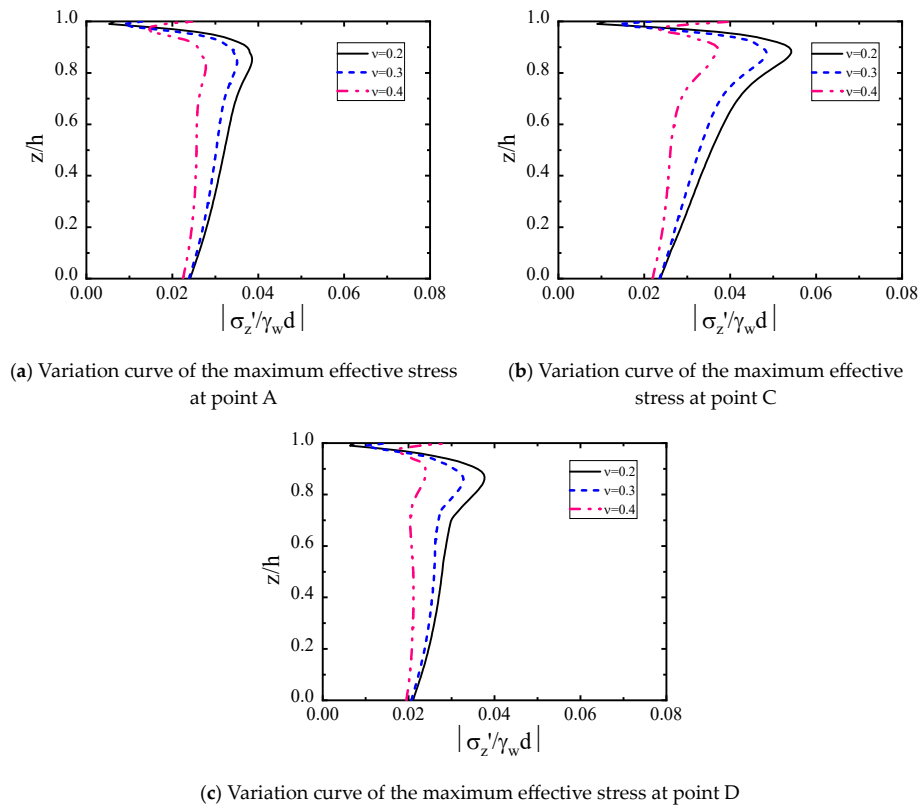


Figure 18. Variation curve of the maximum value of effective stress with depth at each measurement point around the semi-circular breakwater with different Poisson's ratios.

4.4. Geometrical Characteristics of the Semi-Circular Breakwater

The dynamic response of the seabed results from the coupled interaction between the waves, seabed, and structures. Structural dimensional changes can significantly impact the oscillatory response of the surrounding seabed soil [30]. Serving as a novel protective structure, the semi-circular breakwater boasts a distinctive design with an arched shape, and variations in its radius directly influence the reflection and diffraction of waves, thereby affecting the oscillatory response of the seabed. Considering the practical applications, breakwater dimension design is also a crucial consideration. This section focuses on studying the influence of semi-circular breakwater radius variations on the dynamic response of the seabed.

In investigating the influence of the radius of the arched structure, a water depth of 10 m was employed, along with specific radius values of 5 m, 7 m, and 10 m. Additional parameter values are cross-referenced from Table 2. Figures 19 and 20 illustrate the distribution of the maximum pore water pressure and maximum effective stress concerning the seabed depth at different locations around the semi-circular breakwater for different radii. Figure 19 indicates that within the range of $0.8 h < z < h$, the maximum pore water pressure at the same location decreased with increasing seabed depth, exhibiting a reduced decay rate at $z = 0.8 h$. For the range of $0 < z < 0.8 h$, the pore water pressure within this interval was not high, and the maximum pore water pressure remained relatively constant. This was due to the attenuation of wave energy within a water depth of 10 m. As it propagates downward from the seabed surface, the fluid flow encounters frictional resistance with the soil particles, leading to further energy attenuation. It was observed that the maximum pore pressure decreased with an increase in the radius, especially for $R = 10$ m within the top 40% of the seabed depth. This phenomenon arose due to the selected reference points, which are situated below the breakwater and remained relatively unaffected by the wave load from above when the radius increased to 10 m.

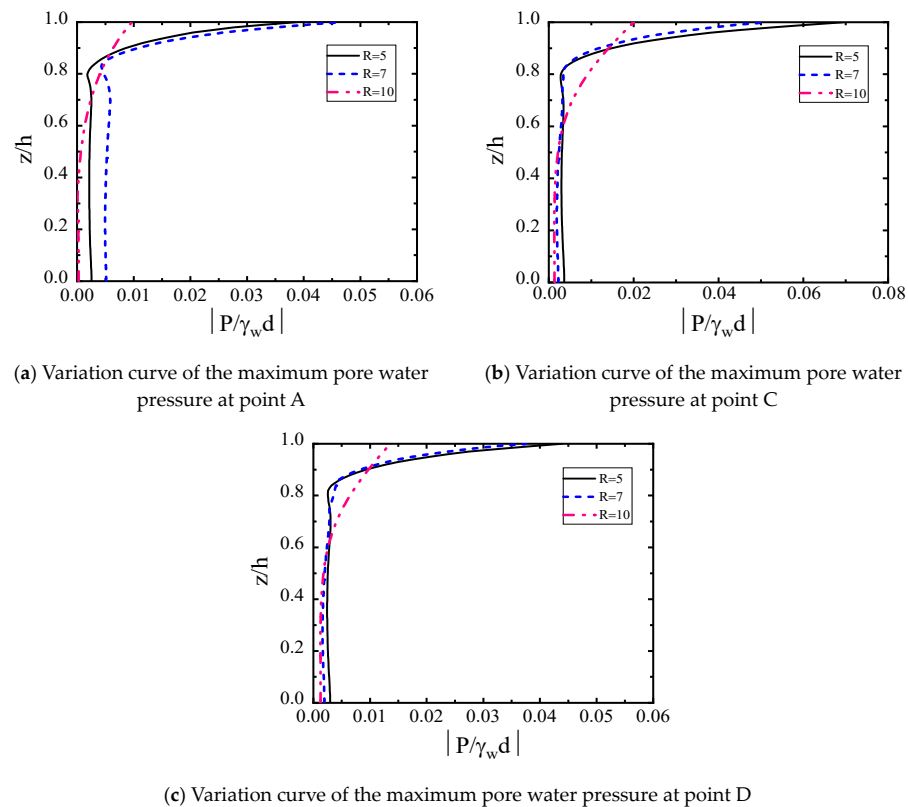


Figure 19. Variation curve of the maximum pore water pressure with depth at each measurement point around the semi-circular breakwater with different radii.

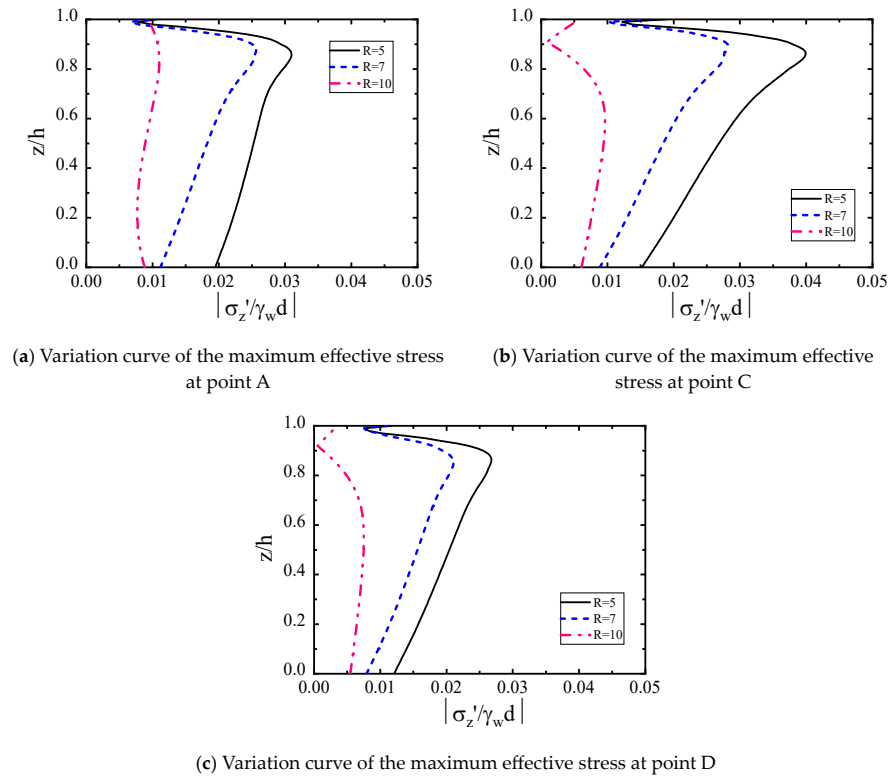


Figure 20. Variation curve of the maximum value of effective stress with depth at each measurement point around the semi-circular breakwater with different radii.

It is evident from Figure 20 that, at the same seabed depth, the maximum effective stress decreased with an increasing radius. Among the three points A, C, and D, point C exhibited significantly higher maximum effective stress compared to the other two points. The dynamic response of the seabed at point D showed the smallest variation. This can be partly attributed to wave reflection and superposition at point C and also to the larger radius of the breakwater, which provides a stronger hindrance to wave propagation.

The tendency of the maximum effective stress for $R = 10$ m was different from that for $R = 5$ m and $R = 7$ m. The reason is that, when the water depth is 10 m, and the radius of the breakwater is 10 m, a part of the breakwater will be exposed to the water surface during wave propagation. This causes a severe increase in wave reflection on the wave-facing side of the breakwater, an increase in wave height, and a decrease in effective stress. The soil below the seabed is less affected by this, so the changes are not significant.

4.5. Liquefaction Depth

Liquefaction is the phenomenon in which the soil changes from a solid state to a liquid state when the excess pore pressure is equal to the effective stress of the overlying soil layer. This leads to a loss of soil strength and stiffness. Seabed liquefaction can be divided into two types: instantaneous liquefaction and residual liquefaction. Instantaneous liquefaction is generated by an oscillating pore pressure and exhibits significant periodicity. Residual liquefaction is caused by the accumulation of excess pore pressure after multiple wave cycles. This article mainly studies instantaneous liquefaction. During wave propagation, the oscillating pore pressure varied periodically with the variation in wave peaks and valleys. The variation in pore pressure along the depth of the seabed can be effectively used to capture wave-induced liquefaction phenomena. Near the wave trough, the vertical gradient of oscillating pore pressure generates upward seepage force. When the excess pore pressure exceeds the effective weight of the soil, instantaneous liquefaction may occur.

In the natural environment, the seabed soil undergoes consolidation over time under the influence of gravity, reaching an initial state of equilibrium. However, the construction

of a breakwater disrupts this initial equilibrium state and generates disturbances in the surrounding seabed. The breakwater and the adjacent seabed foundation enter a new state of consolidation under the influence of gravity [31]. This new equilibrium state is used as the initial state for liquefaction analysis of the seabed in this study.

This section aims to investigate the influence of various parameters (wave characteristics, seabed properties, breakwater characteristics) on the maximum liquefaction depth of the seabed around the semi-circular breakwater. The liquefaction depth is the depth of liquefaction in the vertical direction (i.e., z-direction) of the seabed. Figure 21 presents the variations in the maximum liquefaction depth of the seabed under different wave characteristics, seabed properties, and semi-circular geometries. The rectangular area in the figure represents the location where the semi-circular breakwater and the stone foundation interact. Given that the breakwaters analyzed in this study are all submerged breakwaters, which are more aesthetically appealing than emerged breakwaters, some waves can pass over the breakwater and reach the area behind it, causing disturbances to the soil. Therefore, liquefaction can also occur behind the breakwater. However, the breakwater reflects the waves on its front side, impeding wave propagation. The dynamic response of the seabed soil behind the breakwater is smaller than that on the front side.

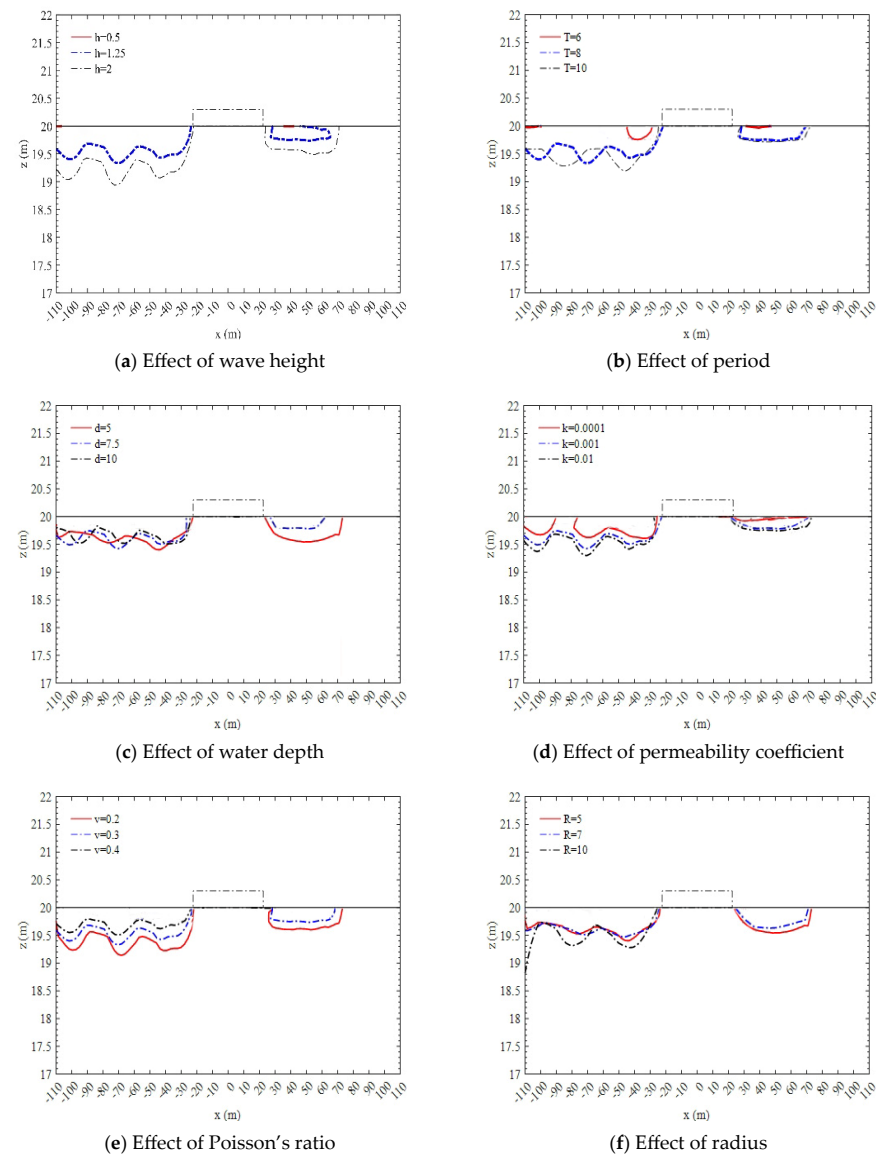


Figure 21. Effect of different parameters on the maximum liquefaction depth of the seabed around a semi-circular breakwater.

The analysis indicated that the maximum liquefaction depth was positively correlated with wave height, wave period, and permeability coefficient, while it was negatively correlated with water depth and Poisson's ratio. Liquefaction almost did not occur when the wave height was 0.5 m. As the wave height increased to 2 m, the maximum liquefaction depth reached 1.0 m. Similarly, as the wave period increased from 6 s to 10 s, the maximum liquefaction depth reached 0.9 m. When the water depth was 0.5 m, the maximum liquefaction depth was 0.8 m. As the water depth increased to 10 m, the maximum liquefaction depth was 0.4 m. This phenomenon occurs because with an increase in water depth, the energy transmitted to the seabed surface from the wave load diminishes, leading to a reduced dynamic response of the soil. The larger the permeability coefficient, the greater the maximum depth of the transient liquefaction. When the permeability coefficients were 0.0001, 0.001, and 0.01 m/s, the corresponding maximum liquefaction depths were 0.4, 0.5, and 0.7 m, respectively. When the Poisson's ratio was 0.2, 0.3, and 0.4, the corresponding maximum liquefaction depths were 0.9, 0.7, and 0.5 m, respectively. Furthermore, as the radius increased to 10 m, the breakwater's ability to obstruct waves strengthened. Only a few waves could pass the breakwater and reach its rear position, resulting in reduced disturbances behind it. Therefore, liquefaction did not occur behind the breakwater. Therefore, when considering enhanced protection in coastal areas, increasing the radius of the breakwater is recommended.

5. Conclusions

This study systematically analyzed the effects of wave parameters, seabed characteristics, and geometric features of a semicircular breakwater on the dynamic response of the surrounding seabed using the established two-dimensional numerical model of wave-breakwater-seabed system. The following conclusions were drawn:

1. The model established in this study can effectively be applied to the study of the oscillatory response in the seabed surrounding a semicircular breakwater. The fluid model accurately simulates wave generation, propagation, and the reflection and superposition phenomena in front of the breakwater. The seabed model captures the oscillatory response of the seabed foundation under dynamic wave loading;
2. The dynamic response of the seabed is influenced by wave characteristics, seabed properties, and the geometric features of the semicircular breakwater. The dynamic response of seabed soil is intensified by increasing wave height, wave period, and permeability coefficient, whereas the dynamic response is weakened by increasing water depth. There is a negative correlation between the radius of the semicircular breakwater and the dynamic response of the seabed, while the influence of the Poisson's ratio is relatively small;
3. Under wave loading, the maximum pore water pressure in the seabed decreases with increasing seabed depth. The attenuation rate of the maximum pore water pressure shows a sudden change in shallow seabed areas, with the peak value occurring within this region. The maximum effective stress in the seabed shows an increasing trend followed by a decrease as the seabed depth increases, with the peak value occurring in the shallow seabed region;
4. The presence of the semicircular breakwater causes changes in the distribution of the pore water pressure near its foundation, with the most intense dynamic response observed at the interface between the breakwater and the rubble foundation.

Author Contributions: Conceptualization, methodology, and funding acquisition, J.L.; writing—original draft preparation and data curation, Y.J.; writing—review and editing, L.C. and M.S.A.; visualization, L.C.; supervision and project administration, H.S.; software and validation, X.L. All authors have read and agreed to the published version of the manuscript.

Funding: This research was funded by Joint Funds of the National Natural Science Foundation of China (Grant No. U2006225); Shandong Provincial Natural Science Foundation (Grant No. ZR2021YQ31); National Nature Science Foundation of China (Grant No. 42277135); and Taishan Scholars Program (Grant No. tsqn202211176).

Institutional Review Board Statement: Not applicable.

Informed Consent Statement: Not applicable.

Data Availability Statement: Data are contained within the article.

Conflicts of Interest: Author Xu Lv was employed by the company China Petroleum & Chemical Corporation. The remaining authors declare that the research was conducted in the absence of any commercial or financial relationships that could be construed as a potential conflict of interest. In the collection, analyses, and interpretation of data, the Joint Funds of the National Natural Science Foundation of China provided assistance; in the writing of the manuscript, Shandong Provincial Natural Science Foundation, National Nature Science Foundation of China, and Taishan Scholars Program provided assistance.

References

- Romya, A.A.; Moghazy, H.M.; Iskander, M.; Abdelrazek, A.M. Performance assessment of corrugated semi-circular breakwaters for coastal protection. *Alex. Eng. J.* **2022**, *61*, 3587–3598. [\[CrossRef\]](#)
- Liu, Y.; Li, H.; Zhu, L. Bragg reflection of water waves by multiple submerged semi-circular breakwaters. *Appl. Ocean. Res.* **2016**, *56*, 67–78. [\[CrossRef\]](#)
- Li, A.; Liu, Y.; Liu, X.; Zhao, Y. Analytical and experimental studies on Bragg scattering of water waves by multiple submerged perforated semi-circular breakwaters. *Ocean. Eng.* **2020**, *209*, 107419. [\[CrossRef\]](#)
- Li, A.; Liu, Y.; Li, H.; Fang, H. Analysis of water wave interaction with a flexible submerged perforated semi-circular breakwater. *Eur. J. Mech.-B/Fluids* **2020**, *79*, 345–356. [\[CrossRef\]](#)
- Oumeraci, H. Review and analysis of vertical breakwater failures—Lessons learned. *Coast. Eng.* **1994**, *22*, 3–29. [\[CrossRef\]](#)
- Lundgren, H. Stability of breakwaters on poor foundation. *Int. J. Rock Mech. Min. Sci. Geomech. Abstr.* **1991**, *28*, 451–454.
- Puzrin, A. Caisson failure induced by liquefaction: Barcelona Harbour, Spain. In *Geomechanics of Failures*; Springer: Dordrecht, The Netherlands, 2010.
- Mizutani, N.; Mostafa, A.; Iwata, K. Nonlinear regular wave, submerged breakwater and seabed dynamic interaction. *Coast. Eng.* **1998**, *33*, 177–202. [\[CrossRef\]](#)
- Mostafa, A.; Mizutani, N.; Iwata, K. Nonlinear wave, composite breakwater, and seabed dynamic interaction. *J. Waterw. Port Coast. Ocean. Eng.* **1999**, *125*, 0733-0950X. [\[CrossRef\]](#)
- Oumeraci, H. Impact loading and dynamic response of caisson breakwaters—Results of large-scale model tests. In Proceedings of the 23rd International Conference on Coastal Engineering, Venice, Italy, 4–9 October 1992; Volume 2, pp. 1475–1488.
- Sumer, B.M.; Fredsøe, J.; Christensen, S.; Lind, M.T. Sinking/floatation of pipelines and other objects in liquefied soil under waves. *Coast. Eng.* **1999**, *38*, 53–90. [\[CrossRef\]](#)
- Mase, H.; Sakai, T.; Sakamoto, M. Wave-induced porewater pressures and effective stresses around breakwater. *Coast. Eng.* **1994**, *21*, 361–379. [\[CrossRef\]](#)
- Jeng, D.; Cha, D.; Lin, Y.; Hu, P. Wave-induced pore pressure around a composite breakwater. *Coast. Eng.* **2001**, *28*, 1413–1435. [\[CrossRef\]](#)
- Elsafti, H.; Oumeraci, H. Analysis and classification of stepwise failure of monolithic breakwaters. *Coast. Eng.* **2017**, *121*, 221–239. [\[CrossRef\]](#)
- Zhang, J.; Song, S.; Zhai, Y.; Tong, L.; Guo, Y. Numerical study on the wave-induced seabed response around a trenched pipeline. *J. Coastal Res.* **2019**, *35*, 896–906. [\[CrossRef\]](#)
- Jeng, D.-S.; Ye, J.-H.; Zhang, J.-S.; Liu, P.-F. An integrated model for the wave-induced seabed response around marine structures: Model verifications and applications. *Coastal Eng.* **2013**, *72*, 1–19. [\[CrossRef\]](#)
- Cui, L.; Jeng, D.-S. Seabed liquefaction around breakwater heads at a river mouth: An integrated 3D model. *Ocean Eng.* **2021**, *242*, 26. [\[CrossRef\]](#)
- Jiang, L.; Zhang, J.; Tong, L.; Guo, Y.; He, R.; Sun, K. Wave Motion and Seabed Response around a Vertical Structure Sheltered by Submerged Breakwaters with Fabry–Pérot Resonance. *J. Mar. Sci. Eng.* **2022**, *10*, 1797. [\[CrossRef\]](#)
- Lee, I.-G.; Kim, D.-H. Load Resistance Factor for Vertical Caisson Breakwater in Korea. *J. Mar. Sci. Eng.* **2022**, *10*, 468. [\[CrossRef\]](#)
- Li, M.-S.; Hsu, C.-J.; Hsu, H.-C.; Tsai, L.-H. Numerical Analysis of Vertical Breakwater Stability under Extreme Waves. *J. Mar. Sci. Eng.* **2020**, *8*, 986. [\[CrossRef\]](#)
- Engelund, F. *On the Laminar and Turbulent Flows of Ground Water through Homogeneous Sand*; Akademiet for de Tekniske Videnskaber: Copenhagen, Denmark, 1953.
- Baquerizo, A.; Losada, M.A.; Smith, J.M. Wave reflection from beaches: A predictive model. *J. Coast. Res.* **1998**, *14*, 291–298.

23. Brunone, B.; Tomasicchio, G.R. Wave kinematics at steep slopes: Second order model. *J. Waterw. Port Coast. Ocean. Engng. ASCE* **1997**, *123*, 5, 223–232. [[CrossRef](#)]
24. Asumadu, R.; Zhang, J.; Hubert, O.-W.; Akoto, A.B. Two-dimensional model of wave-induced response of seabed around permeable submerged breakwater. *Adv. Mech. Eng.* **2019**, *11*, 1687–8140. [[CrossRef](#)]
25. Cui, L.; Jeng, D.; Liu, J. Numerical analysis of the seabed liquefaction around a fixed gravity-based structure (GBS) of an offshore platform and protection. *Coast. Eng.* **2022**, *249*, 110844. [[CrossRef](#)]
26. Asheghabadi, M.S.; Sahafnia, M.; Bahadori, A.; Bakhshayeshi, N. Seismic behavior of suction caisson for the offshore wind turbine to generate more renewable energy. *Int. J. Environ. Sci. Technol.* **2019**, *16*, 2961–2972. [[CrossRef](#)]
27. Asheghabadi, S.M.; Rahgozar, M.A. Finite Element Seismic Analysis of Soil–Tunnel Interactions in Clay Soils. *Iran. J. Sci. Technol.-Trans. Civ. Eng.* **2019**, *43*, 835–849. [[CrossRef](#)]
28. Li, S.; Liu, J.; Yang, Z.; Bao, X.; Wang, F.; Wang, X.; Asheghabadi, M.S. Multiscale Method for Seismic Response of Near-Source Sites. *Adv. Civ. Eng.* **2020**, *2020*, 8183272. [[CrossRef](#)]
29. Asheghabadi, M.S.; Cheng, X. Analysis of Undrained Seismic Behavior of Shallow Tunnels in Soft Clay Using Nonlinear Kinematic Hardening Model. *Appl. Sci.* **2020**, *10*, 2834. [[CrossRef](#)]
30. Chen, W.; Jeng, D.; Chen, W.; Chen, G.; Zhao, H. Seismic-induced dynamic responses in a poro-elastic seabed: Solutions of different formulations. *Soil Dyn. Earthq. Eng.* **2020**, *131*, 106021. [[CrossRef](#)]
31. Huang, Y.; Bao, Y.; Zhang, M.; Liu, C.; Lu, P. Analysis of the mechanism of seabed liquefaction induced by waves and related seabed protection. *Nat. Hazards* **2015**, *79*, 1399–1408. [[CrossRef](#)]

Disclaimer/Publisher’s Note: The statements, opinions and data contained in all publications are solely those of the individual author(s) and contributor(s) and not of MDPI and/or the editor(s). MDPI and/or the editor(s) disclaim responsibility for any injury to people or property resulting from any ideas, methods, instructions or products referred to in the content.